Effects of Ni-P + DLC multilayer coating on cavitation erosion behavior of AlSi10Mg produced by laser powder bed fusion

Maria Beatrice Abrami, Lorenzo Montesano, Marialaura Tocci
University of Brescia, Italy
mariabeatrice.abrami@unibs.it, https://orcid.org/0000-0002-5119-8702
lorenzo.montesano@unibs.it, https://orcid.org/0000-0001-5465-6265
marialaura.tocci@unibs.it, https://orcid.org/0000-0002-7515-0615

Gianluca Di Egidio
University of Bologna, Italy
gianluca.diegidio2@unibo.it, https://orcid.org/0000-0002-5737-6362

Annalisa Pola
University of Brescia, Italy
annalisa.pola@unibs.it, https://orcid.org/0000-0002-0722-6518

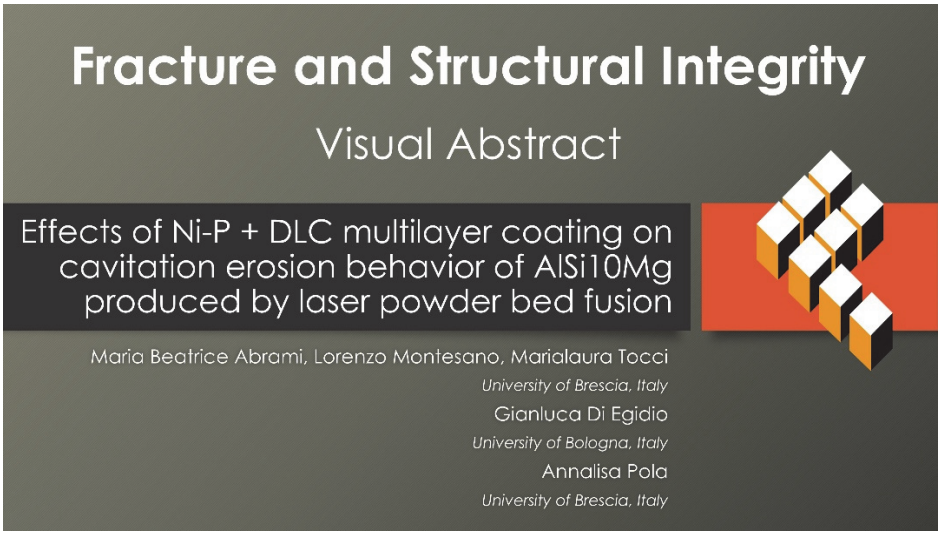

Citation: Abrami, M. B., Montesano, L., Tocci, M., Di Egidio, G., Pola, A., Effects of Ni-P + DLC multilayer coating on cavitation erosion behavior of AlSi10Mg produced by laser powder bed fusion, Fracture and Structural Integrity, 76 (2026) 117-128.

Received: 11.11.2025
Accepted: 14.01.2026
Published: 23.01.2026
Issue: 04.2026

Copyright: © 2026 This is an open access article under the terms of the CC-BY 4.0, which permits unrestricted use, distribution, and reproduction in any medium, provided the original author and source are credited.

KEYWORDS. L-PBF, AlSi10Mg, Hydrogenated amorphous carbon (a-C:H) DLC coating, Electroless Ni-P coating,Cavitation erosion.

INTRODUCTION

In recent years, the use of additive manufacturing (AM) technologies for fabricating complex-shaped components has gained considerable attention, particularly in the context of lightweight design for transport and aerospace industries [1]. Among the various AM methods, laser powder bed fusion (L-PBF) stands out for its effectiveness in producing near-net-shape parts with high geometric complexity [2].

One of the most considered alloys for L-PBF is AlSi10Mg, owing to its good printability, given the high thermal conductivity, low coefficient of thermal expansion and high laser reflectivity [3]. In addition, this alloy has excellent strength-to-weight ratio, as well as high recyclability and low cost, making it attractive in the industrial field, especially for structural and lightweight applications [4]. However, due to its layer-by-layer nature and the use of powder feedstock, L-PBF-produced parts often suffer from intrinsically high surface roughness and limited surface properties, leading to increased susceptibility to damage initiation at the surface [5]. Furthermore, although the hardness of additively manufactured Al alloys is typically higher than that of conventionally produced ones [6], it remains relatively low, still making these alloys susceptible to surface damages.

To address these limitations, various surface post-processing techniques have been explored, including surface treatments (machining, sand-blasting, or shot peening), as well as the application of protective coatings [7, 8]. Electroless Ni-P coatings have been extensively investigated as protective layers for Al alloys and other substrates, due to their high hardness, uniform thickness even on complex geometries, and excellent resistance to wear and corrosion [9]. On the other hand, diamond-like carbon (DLC) coatings have been widely applied on metallic materials for their hardness, low friction coefficient and chemical inertness, which translate into superior wear resistance and corrosion protection [10].

In recent years, a multilayer approach combining Ni-P with DLC has been proposed for AlSi10Mg alloy to exploit the advantages of both coatings, achieving improved properties. The Ni-P layer provides enhanced load-bearing capacity due to its hardness, which is crucial for supporting the outer layer and preventing premature failure, while the topcoat DLC supplies exceptional surface properties both in terms of corrosion and tribological behavior. This strategy has shown promising results in terms of wear, fatigue and corrosion resistance on aluminum alloys [8, 11-14].

On this basis, the Ni-P + DLC multilayer could be an interesting candidate also to enhance AlSi10Mg cavitation resistance, such as for fluid machinery applications, including automotive components. Cavitation erosion occurs when vapor bubbles form and collapse at a component surface, producing rapid pressure changes. In machinery operating with high-speed fluid flows, local pressure drops can lead to vapor formation, which collapse as the pressure rises again. The implosion of vapor bubbles generates shock waves and micro-jets, which can induce surface fatigue, crack initiation, and progressive material removal [15, 16]. A key factor in improving resistance to cavitation is increasing surface hardness, which can be effectively achieved through the application of protective coatings. In this regard, previous studies have highlighted the improvement of cavitation resistance on different alloy substrates through the application of Ni-P [17-19] or DLC [20-23] coatings. However, the potential of using a multilayer approach combining both has not yet been explored, which constitutes the aim of the current investigation.

MATERIALS AND METHODS

AlSi10Mg plates of 32 x 30 x 4 mm were produced with a EOSINT M270 Dual Mode, a laser powder bed fusion system, using the optimized parameters summarized in Tab. 1. Commercial AlSi10Mg powder were used, with a powder size distribution ranging from 20 to 63 μm. The chamber was filled with Ar atmosphere (O<0.1%). The platform was pre-heated at 100 °C, and the printing strategy consisted of stripes with 67° rotation. After printing, a stress relieving heat treatment at 270 °C for 90 minutes was performed.

Layer thickness	Laser power	Scan speed	Hatch distance
30 μm	195 W	800 mm/s	170 μm

Table 1: Process parameters used to build AlSi10Mg samples.

The multilayer coating consists of: (i) electroless Ni-P interlayer, and (ii) hydrogenated amorphous carbon (a-C:H) topcoat. Before multilayer deposition, a tumbling process was performed to reduce surface roughness and a final light manual polishing was performed to reduce surface inhomogeneities. A "medium phosphorus" Ni-P coating (9 wt.%) was chosen to be deposited in an industrial environment (from the liquid phase, at approximately 90 °C) for the optimal combination of corrosion resistance and mechanical/tribological properties. The DLC (amorphous hydrogenated carbon, a-C:H) topcoat was also deposited in an industrial environment via Plasma-Assisted Chemical Vapor Deposition (PA-CVD). The DLC was deposited from the vapor phase at about 150-180 °C. Further processing details for the whole cycle cannot be disclosed.

A preliminary characterization was carried out on the cross-sections of the coated samples to determine the coating thickness. The samples were sectioned, mounted, polished to mirror finish, and subsequently examined using both an optical microscope Leica DMI 5000M and a field emission scanning electron microscope (FEG-SEM, Zeiss Sigma 360). The

adhesion of the Ni-P and Ni-P + DLC coatings was previously evaluated in [14], showing overall good adhesion for both layers.

Cavitation tests were carried out following the "stationary specimen method", illustrated in the ASTM G32-16 standard [15]. The experiments were performed on uncoated AlSi10Mg alloy, and on the same alloy coated with either a single Ni-P layer or Ni-P + DLC multilayer, hereafter referred to as AlSi10Mg, Ni-P and Ni-P + DLC samples, respectively. An ultrasonic device (Felisari GV2000) with a vibration frequency of 20 kHz, vibration amplitude of 50 μm and electrical peak power of 2 kW was used. The ultrasound probe (sonotrode) was made of a Ti6Al4V waveguide and an Inconel 625 horn with a final amplification diameter of 18 mm. Samples were inserted in a proper holding system, immersed in a tank containing distilled water, with one of the surfaces exposed at 0.50 mm distance from the sonotrode tip. Water temperature was maintained at 25 ± 2 °C. For each condition, three samples were tested for a total test duration of 8 hours. To evaluate the improvement of the coatings with respect to the as-built condition as the scope of the work, the surface of the AlSi10Mg was tested without being polished. Tests were periodically interrupted to examine the morphology of the eroded surface using a DMS300 digital microscope and a digital scanner. The weight loss of the whole samples was measured using a scale with an accuracy of 0.1 mg. Weight loss data were used to obtain cumulative mass loss (also named cumulative erosion) as function of time. According to the standard the data collected were also processed in order to obtain incubation time. Furthermore, the instantaneous erosion rate was calculated by numerical differentiation of the cumulative mass loss-time curve. The damaged surfaces were observed by FEG-SEM after selected periods of cavitation exposure. Finally, after cavitation tests, one of the Ni-P+DLC samples was sectioned across the eroded area, ground, and polished for FEG-SEM observation to further investigate the damage mechanisms.

RESULTS AND DISCUSSION

Fig. 1 shows a polished cross-section of the Ni-P + DLC coated sample, while Tab. 2 reports the corresponding EDX analyses. The multilayer system is composed of a phosphorus electroless Ni-P layer (Spectrum 3, Tab. 2) with an average thickness of approximately 20 μm, topped by a DLC coating consisting of a Cr-rich interlayer (Spectrum 2, Tab. 2) and a C-rich outer layer (Spectrum 1, Tab. 2), with a combined thickness of approximately 4 μm. The multilayer also contains an element X, whose identity cannot be disclosed. The Ni-P single-layer sample features the same electroless Ni-P coating as the base layer of the multilayer system, but without the upper DLC deposition.

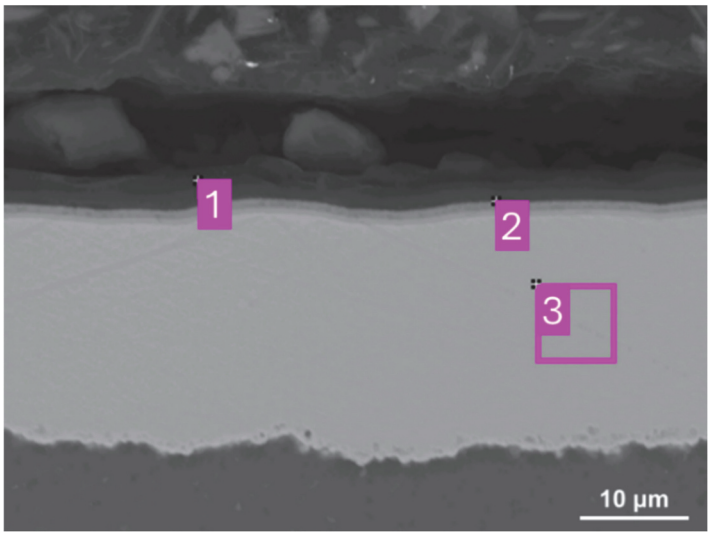

Figure 1: Cross-sectional view of the Ni-P + DLC multilayer coating on AlSi10Mg.

Spectrum	C	O	X	P	Cr	Ni
1	89.10	2.17	7.33		1.40	
2	29.97		9.64		54.50	5.89
3				7.90		92.10

Table 2: EDX analyses (wt.%) of the areas shown in Fig. 1.

The overall qualitative view of the cavitation damage evolution is shown in Fig. 2 for representative AlSi10Mg, Ni-P and Ni-P + DLC samples at selected times.

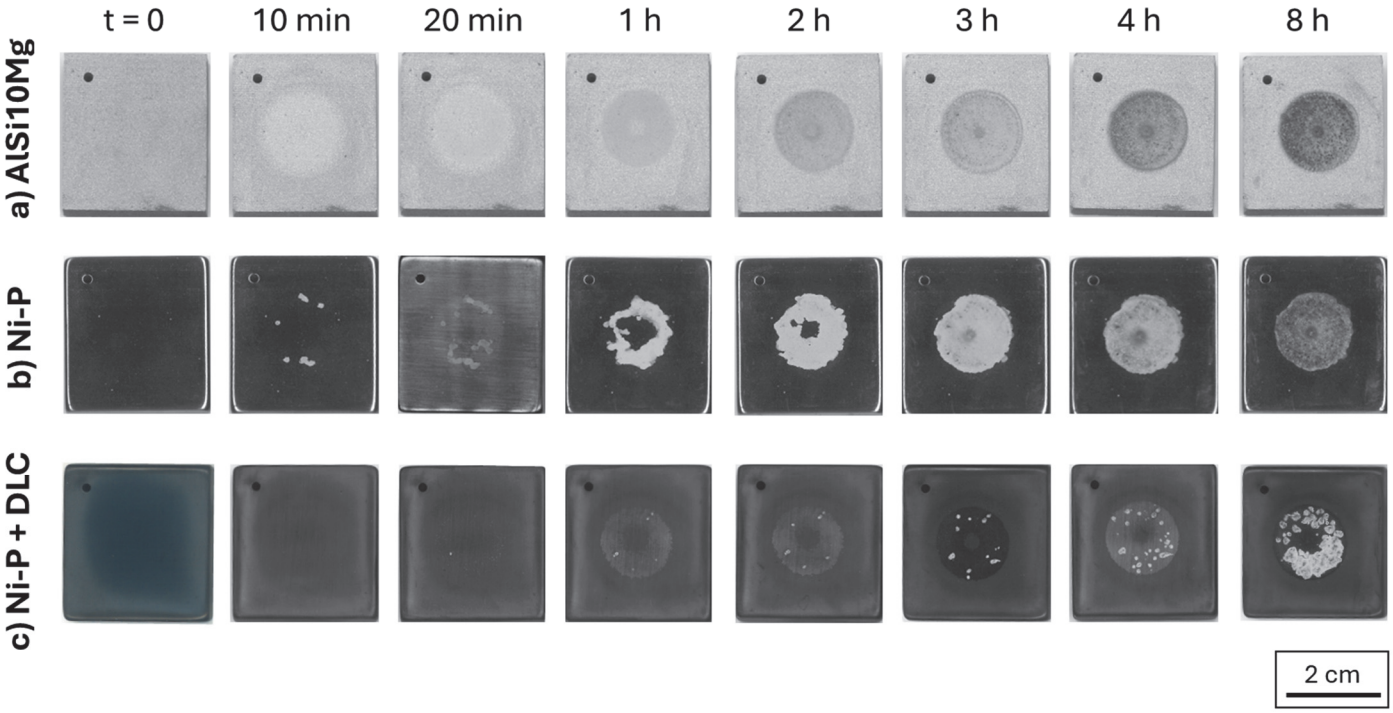

Figure 2: Qualitative cavitation damage evolution for a) AlSi10Mg, b) Ni-P and c) Ni-P + DLC.

The AlSi10Mg alloy damages rapidly, with the eroded area becoming visible within the first 10 min and progressively deepening and widening with time (Fig. 2a). The damaged surface presents a uniform ring-like shape, characteristic of the stationary specimen method of cavitation erosion tests, that reflects the cylindrical shape of the ultrasonic field [16, 24]. Its formation originates from the progressive plastic deformation induced by cavitation micro-jets and shock waves, which becomes more evident as the testing time increases. Concerning the Ni-P sample, the erosion phenomenon starts with localized coating removal in several areas, where the underlying Al-substrate is revealed (Fig. 2b, 10 min). Then, erosion propagates rapidly, enlarging the areas where the coating has previously detached, as well as simultaneously generating new uncoated areas. As a result, after 1 h the underlying Al-substrate becomes widely exposed. The damaged area becomes then more uniform as the exposure time increases (Fig. 2b, 3 h), resulting in a ring-like shape, similarly to the uncoated sample. During the cavitation erosion of Ni-P + DLC, the surface remains intact in the early stages. The DLC layer exhibits slight localized damage, characterized by very small spots where the underlying layers become visible (Fig. 2c, 20 min). After 1 h of exposure, the DLC coating is almost completely removed, forming a uniform ring mainly exposing the Ni-P layer (light grey ring), along with limited areas where the Al-substrate emerges (lighter spots). After 3 h, erosion of Al-substrate becomes more evident, progressing in the previously exposed areas. At the end of 8 h exposure time, the damaged surface is non uniform, consisting mostly of areas revealing the Al-substrate, together with limited regions where the Ni-P layer is still present. It should be noted that the erosion of both Ni-P and Ni-P + DLC samples starts with the damage of the coatings in localized areas and then progresses not only in the surrounding coating, but also within the areas where the coating was already removed, thus further exposing and damaging the underlying layers. As a result, the coating and the substrates experience simultaneous cavitation erosion, making it not realistically possible to accurately determine the mass loss of the coating alone [23].

Fig. 3 shows the interface between the eroded area and the undamaged region at the end of the cavitation test, observed by digital microscopy. For the AlSi10Mg alloy (Fig. 3a), the damaged area appears homogeneous, with a compact eroded region, typical of cavitation-induced plastic deformation and material loss. For the Ni-P coated sample (Fig. 3b), the coating is completely removed within the damaged area, exposing the underlying Al substrate, which itself appears eroded. The damage seems to propagate beyond the main eroded zone, as indicated by the lighter regions marked by arrows, corresponding to Al. These areas were not directly affected by cavitation, as evidenced by their smooth morphology and location outside the exposed region, suggesting that their damage originated from the detachment of the surrounding Ni-P coating subjected to cavitation. The Ni-P + DLC system (Fig. 3c) shows a markedly different morphology, with more damaged islands (lighter

areas) exposing the underlying Al substrate distributed along the erosion ring, while the rest of the area is still coated by Ni-P.

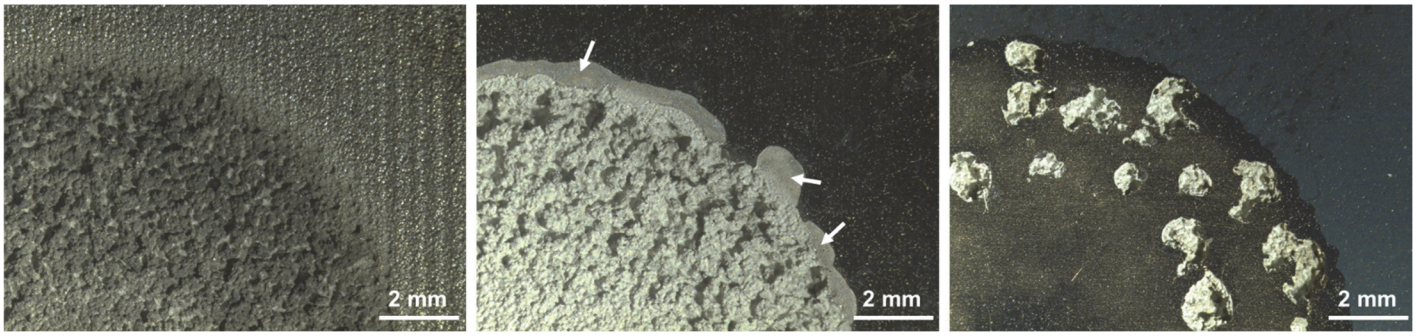

Figure 3: Cavitation damage at the end of the test for: a) AlSi10Mg, b) Ni-P and c) Ni-P + DLC samples.

Fig. 4 displays the cumulative mass loss as a function of the exposure time for representative AlSi10Mg, Ni-P and Ni-P + DLC samples. Due to the simultaneous and progressive erosion of the coatings and the underlying layers, the reported mass loss is to ascribe to the entire system, rather than the coatings themselves. For the same reason, the data are presented in terms of mass loss rather than calculating volume loss, and the mean depth of erosion was not determined, since it is not possible to separate the contribution of each layer during the progress of erosion. A magnification of the first part of each curve is reported to better visualize the incubation time, which was determined as the x-intercept of the straight-line extension of the maximum slope portion of the cumulative erosion-time curve. The slope of this line corresponds to the erosion rate. For the Ni-P + DLC sample, two maximum slope portions were detected and are highlighted in Fig. 4c. Considering that the sample consists of both the substrate and the multilayer coating, it is reasonable to assume that the first change in slope (referred to as incubation 1) corresponds to the incubation time of the DLC coating, as also suggested by the limited weight loss without evident surface damage (Fig. 2c, 10-20 min). Conversely, the second maximum slope (incubation 2) marks the onset of more severe damage, which can be mainly attributed to the substrate. This is evident referring to Fig. 2c, where the damage of the Al-substrate becomes predominant after approximately 3 h, which is consistent with the second incubation period. Tab. 3 displays the incubation times and the erosion rates for each condition.

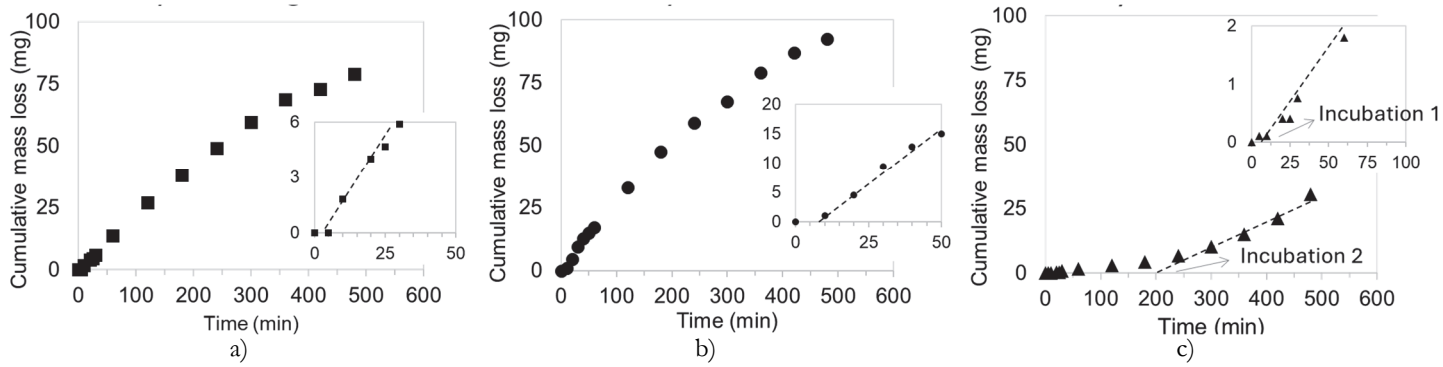

Figure 4: Cumulative mass loss as function of time for a) AlSi10Mg, b) Ni-P and c) Ni-P + DLC. A magnification of the initial part of the curves pointing out the incubation time is also reported.

Cavitation parameter	AlSi10Mg	Ni-P	Ni-P + DLC	
			Incubation 1	Incubation 2
Incubation time (min)	5 ± 4	6 ± 3	12 ± 3	228 ± 14
Erosion rate (mg/min)	0.23 ± 0.03	0.54 ± 0.20	0.04 ± 0.01	0.17 ± 0.09

Table 3: Incubation times for the tested samples.

The uncoated AlSi10Mg exhibits rapid and nearly linear mass loss with a very short incubation period, indicating the immediate onset of material removal. The incubation time of the Ni-P coated samples is comparable to AlSi10Mg, indicating

that the presence of the Ni-P layer does not significantly delay the onset of erosion. As previously pointed out, the Ni-P + DLC multilayer coating displays two-stage incubation behavior. The first incubation period reflects the onset of damage to the DLC coating, while the second relates to the underlying Al-substrate. The Ni-P + DLC sample shows a longer incubation time than the others, highlighting the protective role of the DLC topcoat that postpones the initiation of erosion. Furthermore, the damage of Al-substrate occurs predominantly after approximately 3 h, pointing out that the protective action of the multilayer is much longer than the Ni-P coating alone.

Interestingly, the Ni-P coated sample exhibits higher erosion rate compared to that of the uncoated AlSi10Mg (Tab. 3). This can be attributed to the rapid removal of the Ni-P layer once cavitation damage initiates, due to detachment of coating fragments (Fig. 2b). The higher standard deviation of the Ni-P erosion rate reported in Tab. 3 points out that the erosion behavior of this sample is highly sensitive to surface or subsurface defects. This is further supported by the evolution of cavitation erosion observed in Fig. 2b, where the damage appears localized in scattered areas, suggesting that these were more susceptible to erosion due to pre-existing defects. The number of these initiation sites was observed to vary significantly across different test repetitions. The Ni-P + DLC coated sample displays significantly lower erosion rate related to the first incubation period. This is indicative of the enhanced protective capability of the multilayer system, due to the higher surface hardness of the DLC layer combined with the superior load-bearing capacity of the underlying Ni-P coating. After the second incubation, the erosion rate remains below that of Ni-P, demonstrating the stronger resistance provided by the multilayer system compared to the single layer. Furthermore, Ni-P + DLC second erosion rate is comparable to the one of AlSi10Mg, confirming that after the second incubation time the main damage is related to underlying substrate, as discussed above.

The instantaneous erosion rate-time curve obtained by numerical differentiation of the cumulative erosion-time curve is reported in Fig. 5 for each condition.

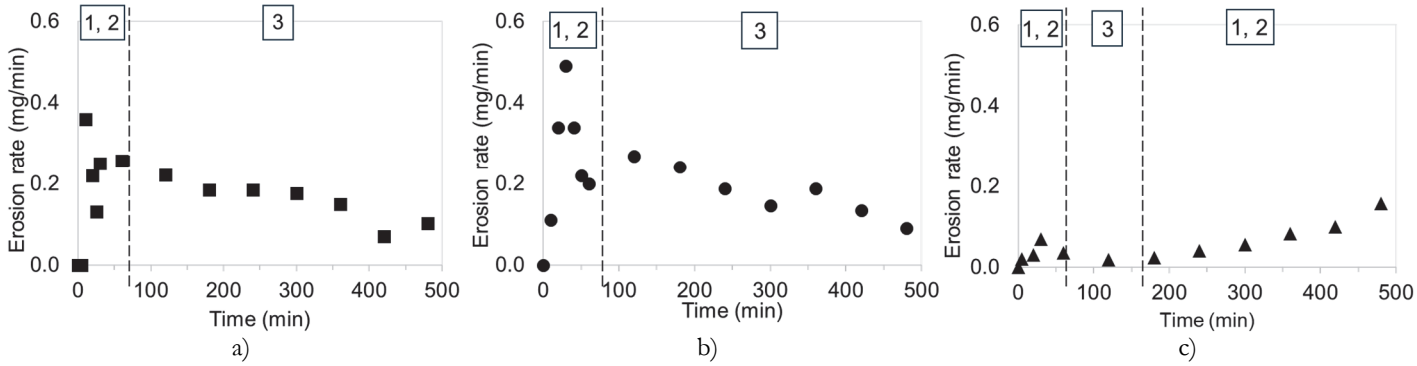

Figure 5: Instantaneous erosion rate as function of time for a) AlSi10Mg, b) Ni-P and c) Ni-P + DLC.

The characteristic stages of cavitation erosion can be identified, which are: (1) incubation, (2) acceleration stage and maximum erosion rate, and (3) deceleration and terminal stage, if present [15]. During the incubation period, the erosion rate is zero or negligible with respect to the following stages. This phase corresponds to the accumulation of plastic deformation and internal stresses under the surface, preceding the significant material loss [15]. Then, during the acceleration period, an increase in the erosion rate is recorded. As previously pointed out, AlSi10Mg and Ni-P samples show a short incubation phase, transitioning almost immediately to the acceleration stage. Both the samples exhibit a deceleration and terminal stage, where a final steady-state is reached. Concerning the Ni-P + DLC coating, after an initial incubation and acceleration stage, an intermediate deceleration stage is reached until around 3 h, with a subsequent further increase of the erosion rate, representing another incubation and acceleration stage. The trend of the curve suggests that the second peak of the maximum erosion rate is not reached by the Ni-P + DLC sample within the examined time interval, and neither the final deceleration nor the terminal phase. As previously discussed, the second incubation and acceleration stage can be mainly ascribed to the Al-substrate (Fig. 2c, 3 h). In this regard, the incubation period of Al alloy is significantly extended, indicating higher resistance to initial cavitation damage. The subsequent acceleration stage for the Al-substrate is delayed and moderate in terms of instantaneous erosion rate as it reflects the damage of limited fraction of surface where the coating has been already removed.

The total mass loss was 91 ± 24 mg for AlSi10Mg, 123 ± 43 mg for the Ni-P coated sample, and 44 ± 19 mg for the Ni-P + DLC coated sample. The Ni-P coated sample shows even higher mass loss than the uncoated alloy, which may be due to the detachment of large coating fragments combined with the higher density of Ni-P (about 8.1 g/cm^3 [9]), resulting in a

greater mass loss. In contrast, the Ni-P + DLC system shows a limited mass loss, confirming the beneficial effect of the DLC topcoat in both delaying the onset of erosion and reducing the overall material removal of the system.
The cavitation erosion damaging mechanisms were investigated by means of digital microscopy and FEG-SEM.
Fig. 6 displays FEG-SEM images at the incubation time and after the incubation time for AlSi10Mg alloy. The surface of the uncoated AlSi10Mg sample at the incubation time shows early signs of plastic deformation, with the presence of some small cracks (evidenced by white arrows in Fig. 6a), due to the collapse of vapor bubbles that produce micro-jets and shock waves. These microscopical modifications appear during the incubation step, initially without any loss of material, while then they result in the onset of material removal. After incubation, the damage progresses with propagation of larger cracks resulting in material removal (Fig. 6b). This is in agreement with the typical cavitation erosion mechanism of metallic materials [16].

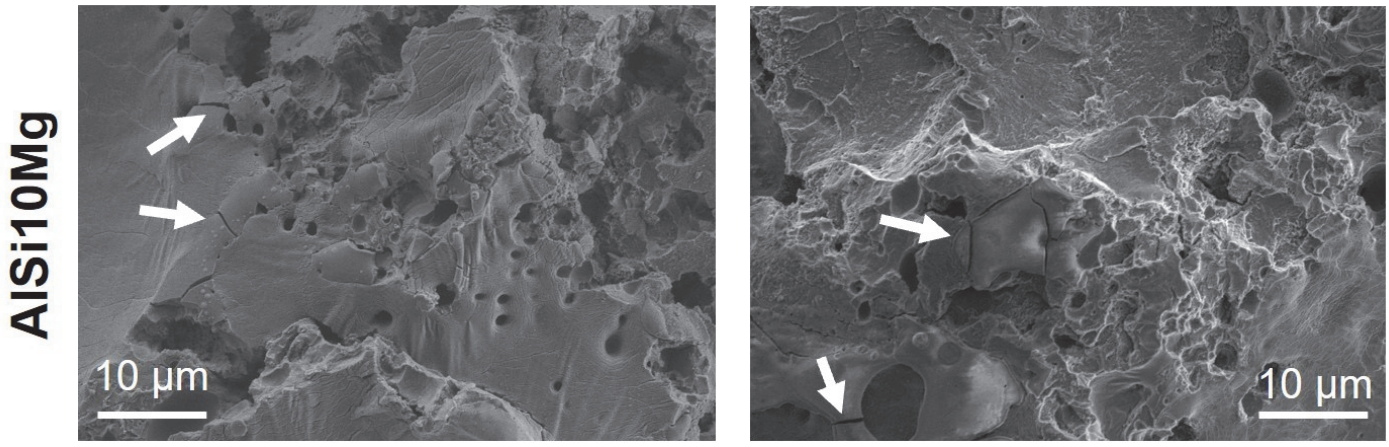

Figure 6: Top-view images of AlSi10Mg sample at different exposing stages: a) incubation time, b) after incubation.

The erosion evolution for Ni-P coated sample is displayed in Fig. 7, while the corresponding EDX analyses are reported in Tab. 4. Before the incubation, small pre-existing discontinuities emerging from the polished surface can be detected (Fig. 7a). The underlying morphology, visible in the magnification of Fig. 7a, is the characteristic dome-like geometry of Ni-P, which results from the autocatalytic liquid-phase deposition. At the incubation time, Ni-P sample shows the starting of coating detachment in some areas (Fig. 7b), exposing the substrate. The coating detachment is brittle, as can be seen by the presence of cracks in the remaining surrounding coating. Likely, detachment started from the discontinuities shown in Fig. 7a. After incubation (Fig. 7c), the coating adjacent to the erosion front appears uplifted and characterized by a wavy morphology, as indicated by the arrows. This morphology indicates progressive delamination between the remaining Ni-P coating and the substrate, as previously seen in Fig. 3b.

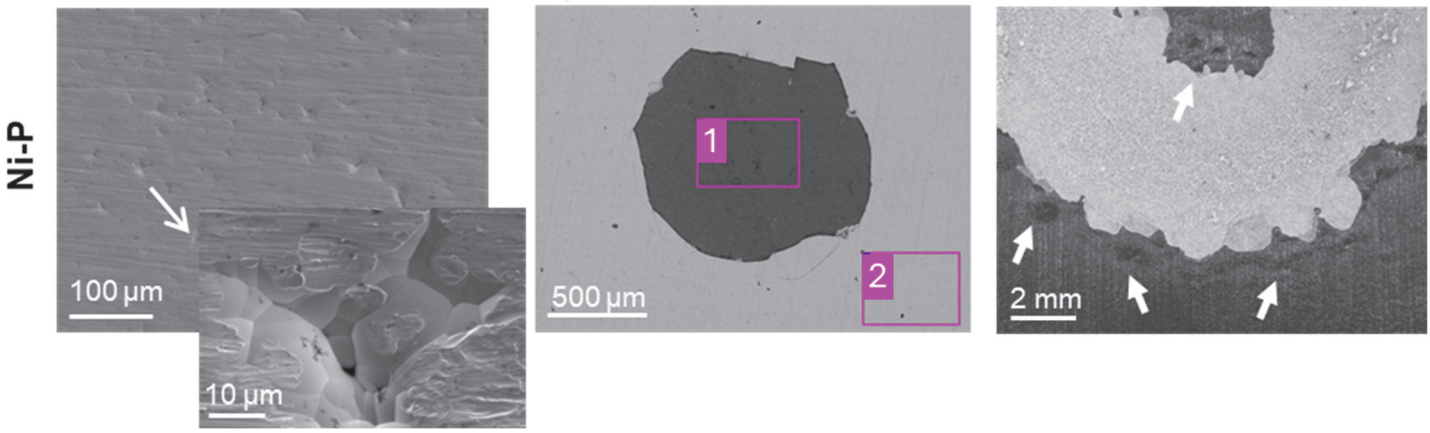

Figure 7: Top-view micrographs of Ni-P sample at different exposing stages: a) before incubation, b) incubation time (FEG-SEM images), c) after incubation (digital microscope image).

Spectrum	O	Al	Si	P	Ni
1	8.70	81.02	10.28		
2				10.18	89.82

Table 4: EDX analyses (wt.%) of the areas shown in Fig. 7.

For the Ni-P + DLC multilayer, FEG-SEM images shown in Fig. 8 are presented at the first incubation time, representative of the damaging of the DLC topcoat. The corresponding EDX analyses are listed in Tab. 5. Similarly to the Ni-P coating, the DLC layer at this stage begins to detach (Fig. 8a,b). However, the affected areas are significantly smaller compared to the Ni-P single layer coating, as also seen from Fig. 2. The detachment originates from the underlying Ni-P layer as displayed in Fig. 8a, where its dome-like morphology is clearly visible. The DLC replicates in fact the Ni-P morphology (magnification of Fig. 8a). These spots where the coating starts to detach likely correspond to the small discontinuities seen in Fig. 7a for the Ni-P coated sample. On the other hand, Fig. 8b reveals a region where the Ni-P layer did not fully cover the substrate, resulting in a localized void in which the DLC deposited (Fig. 8b and Spectrum 1, Tab. 5). Both the areas in Fig. 8 correspond to sites where the DLC deposition may have been less effective, either due to discontinuities of the Ni-P morphology or to its local absence, resulting in reduced topcoat adhesion. This made these locations preferential sites for DLC detachment during cavitation exposure, similarly to what previously observed for the Ni-P coating. In this case, however, the damage was contained. Previous studies also have identified debonding as a primary failure mechanism under cavitation erosion of DLC coating [21, 22].
Finally, it is observed from the magnification of Fig. 8a that DLC coating exhibits a smaller globular morphology, usually referred to as cauliflower-type [8, 25], as a result of the PA-CVD deposition.

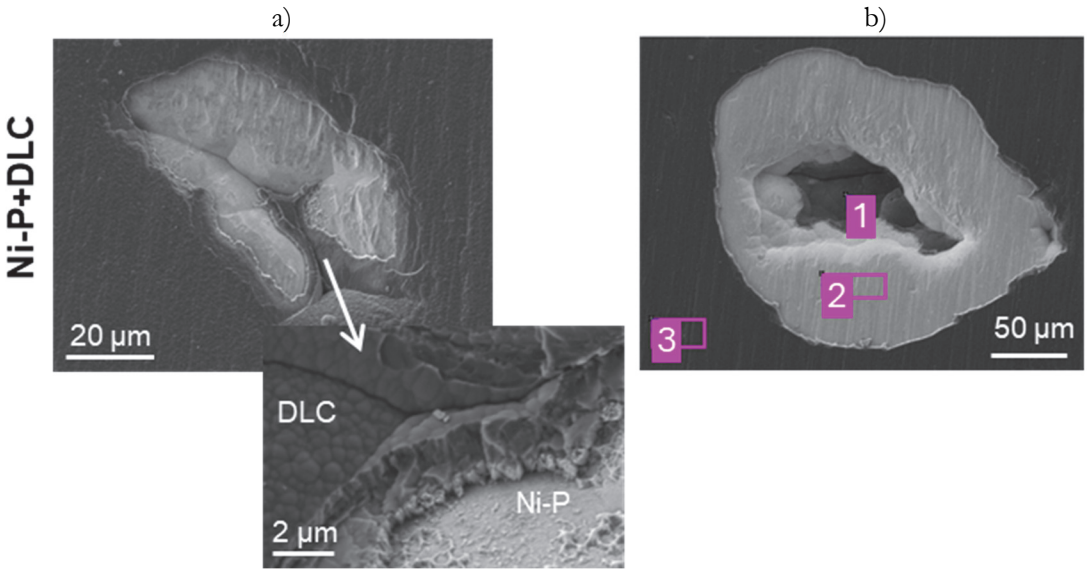

Figure 8: Top-view images of Ni-P + DLC sample: a,b) incubation 1.

Spectrum	C	X	P	Ni
1	84.07	2.79	1.81	11.31
2			8.85	91.15
3	98.31	1.69		

Table 5: EDX analyses (wt.%) of the areas shown in Fig. 8.

Fig. 9 reports top-view FEG-SEM images of the Ni-P + DLC sample after cavitation exposure. The corresponding EDX analyses are shown in Tab. 6. As previously pointed out in Fig. 2c, the Ni-P + DLC sample exhibits a heterogeneous surface, with regions where the Ni-P interlayer is still present (Fig. 9c, Spectrum 2 of Tab. 6) and areas where the coating has been completely removed, exposing the Al-substrate (Fig. 9b, Spectrum 1 of Tab. 6). The DLC top layer was found to persist only in a few isolated regions. The bare Al-substrate (Fig. 9b) shows severe surface roughening and extensive material removal, typical of the advanced cavitation erosion stage of aluminum alloys. Once the DLC has detached, the damage

evolution for the Ni-P + DLC sample proceeds similarly to that observed for the Ni-P coated sample, with cavitation erosion damage localized in regions of Ni-P morphological discontinuities (compare Fig. 9c with Fig. 7a).

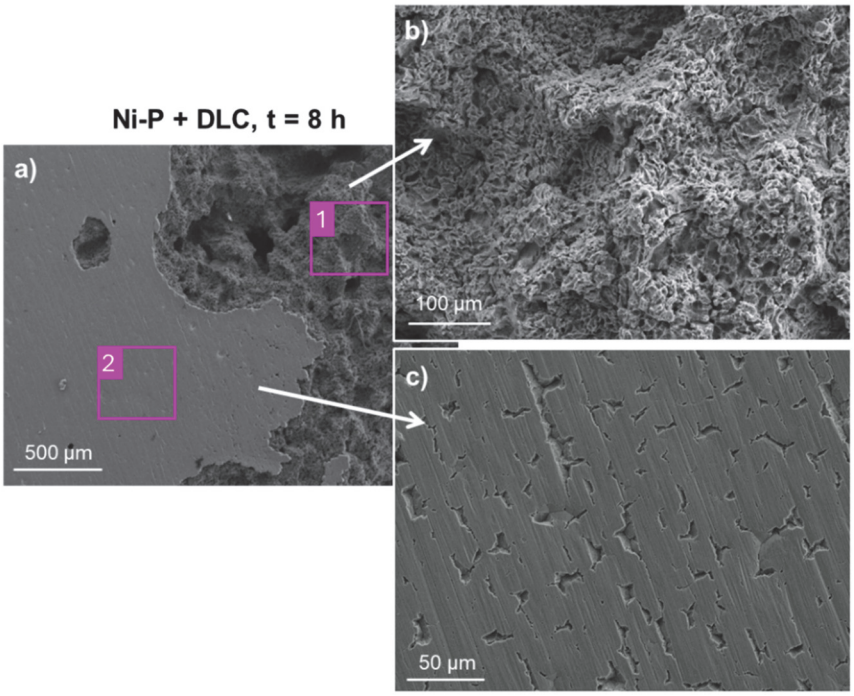

Figure 9: Top-view of Ni-P + DLC sample at the end of the test.

Spectrum	Al	Si	P	Ni
1	88.96	11.04		
2			8.80	91.20

Table 6: EDX analyses (wt.%) of the areas shown in Fig. 9.

Fig. 10 shows the cross-sections of Ni-P + DLC coated samples after 8 h of cavitation erosion exposure. The DLC top layer is no longer detectable, revealing areas consisting of the underlying Ni-P coating or the Al substrate. The remaining Ni-P, exposed to cavitation, exhibits surface-initiated cracking that propagates through its thickness. Once these cracks reach the substrate, the Ni-P layer detaches in fragments, leaving the Al substrate exposed. This indicates that the damage in the Ni-P coating starts from its surface, in regions likely corresponding to the pre-existing defects previously observed in surface analyses.

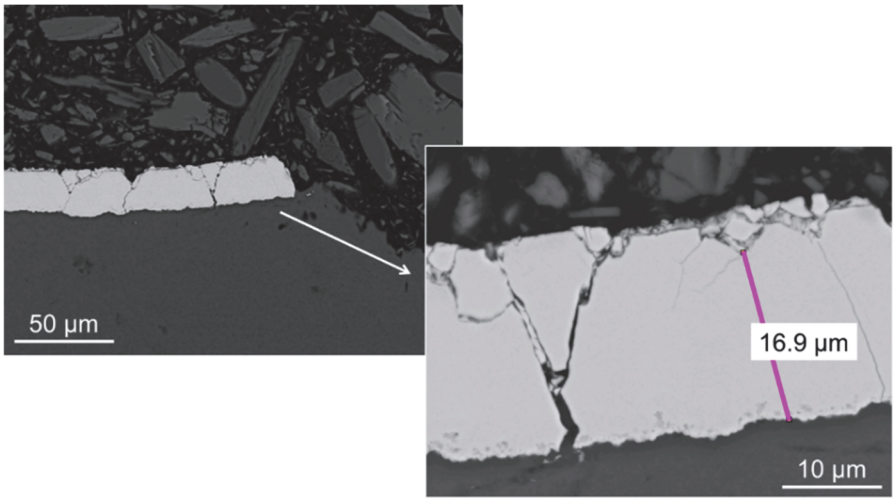

Figure 10: Cross-sectional view of Ni-P + DLC sample at the end of the test.

In general, the damage of the Ni-P and Ni-P + DLC coatings originates from the surface, where cavitation bubbles can form into preexisting micro-cracks or small surface imperfections [21]. For the Ni-P sample, these may correspond to regions exhibiting morphological discontinuities in the layer (Fig. 7a). In the Ni-P + DLC sample they may relate to areas reflecting underlying defects, such as voids (Fig. 8b) or the same discontinuities in the Ni-P layer (Fig. 8a, Fig. 9c). Here, vapor bubbles growth or collapse, eventually causing coating detachment and leading to material removal. In these small areas, bubble collapsing can generate high water pressures [26], promoting crack propagation and the formation of deep grooves (Fig. 9c). If micro-cracks are very shallow, grooves do not reach the substrate that thus will remain protected. Conversely, if grooves are large enough, they will reach the substrate that becomes exposed to the environment [21]. As grooves become numerous and larger, they can coalesce, leading to the detachment of large coating fragments (Fig. 7b, Fig. 8a-b, Fig. 10). This can also cause the surrounding coating to flake off, as mainly seen for Ni-P coating (Fig. 3b, Fig. 7c). A possible strategy to mitigate this damage mechanism is the improvement of the surface finishing prior and after deposition of Ni-P and DLC layers, as also highlighted in [14].

Ni-P uplifting during erosion progression can be due to the cavitation bubbles impinging the exposed Al-substrate, that deforms and damages more easily than the coating. Therefore, since the substrate undergoes greater plastic deformation, the remaining surrounding coating cannot follow the substrate deformation and consequently lifts. The mechanism described also explains the large Ni-P fragments removed from the substrate, and thus the higher erosion rate of Ni-P coated sample compared to the others. This mechanism is mitigated in the Ni-P + DLC sample. In this system, the underlying Ni-P layer provides higher mechanical support compared to the Al substrate, reducing plastic deformation under cavitation. Moreover, the harder DLC top layer delays crack initiation and prevents premature fracture of the Ni-P layer. As a result, the overall damage progression is slower and the erosion rate significantly lower.

According to the literature, the higher erosion rate of Ni-P coated sample compared to the uncoated AlSi10Mg can also be explained by the combined action of cavitation and slurry erosion once the coating delaminates [26], due to the suspension of detached particles in water, that will increase as the test time increases [27, 28]. In fact, once these particles detach, remain suspended in the fluid and, together with the turbulent flow generated by bubble collapse, act as erosive particles. The simultaneous action of cavitation and particle impacts causes localized plastic deformation and material removal on the substrate surface. Over time, repeated bubble collapse and impacts of these suspended particles result in progressive material removal and mass loss. Therefore, despite the protective role of the coating, large fractions of detached coating likely contributed to intensify substrate erosion, as the harder Ni-P fragments impact the softer Al-substrate. An increase in erosion rate is not observed for the Ni-P + DLC multilayer coating, indicating that this phenomenon is contained since the DLC topcoat delays severe detachment and thus limits the generation of hard debris.

CONCLUSIONS

The Ni-P + DLC multilayer significantly enhances the cavitation resistance of AlSi10Mg alloy, as evidenced by the longer incubation time and lower erosion rate compared to uncoated and Ni-P single-layer samples. The enhanced performance is mainly attributed to the multilayer design, where the Ni-P layer increases the load-bearing capability and the DLC top layer provides higher hardness. In contrast, the Ni-P coating alone can exhibit higher erosion rate and mass loss than the uncoated alloy, due to the detachment of large coating fragments during cavitation, which likely act as abrasive particles and contribute to additional surface damage. In both Ni-P single layer and Ni-P + DLC multilayer, damage was found to origin from surface discontinuities and defects. Despite these, the Ni-P + DLC coating proved effective in delaying substrate damage, thereby offering superior protection to AlSi10Mg components operating in cavitating environments.

FUNDING

This work was carried out within the project *Proof of Concept* "ALuminium alloy COmponents produced by additive Manufacturing: financed by the European Union-NextGenerationEU (National Sustainable Mobility Center CN00000023, Italian Ministry of University and Research Decree n. 1033-17/06/2022, Spoke 11-Innovative Materials & Lightweighting), and National Recovery and Resilience Plan (NRRP), Mission 04 Component 2 Investment 1.5-NextGenerationEU, Call for tender n. 3277 dated 30 December 2021.

CONFLICTS OF INTEREST

The authors declare no conflict of interest related to this work.

ACKNOWLEDGEMENTS

The authors deeply thank Dr. Francesco Lavalle and Paolo Lavalle of STS Srl – Cellatica (BS) for the definition of the deposition of the investigated coatings, Dr. Alessandra Martucci and Prof. Mariangela Lombardi of the Polytechnic of Turin for samples production and Mr. Leonardo Lauri of the University of Brescia for contributions to FEG-SEM analysis.

REFERENCES

[1] Ahn, D.G. (2016). Direct metal additive manufacturing processes and their sustainable applications for green technology: A review, Int. J. Precis. Eng. Manuf. Green Technol., 3(4), pp. 381–395. DOI: https://doi.org/10.1007/s40684-016-0048-9

[2] Chowdhury, S., Yadaiah, N., Prakash, C., Ramakrishna, S., Dixit, S., Gupta, L.R., and Buddhi, D. (2022). Laser powder bed fusion: A state-of-the-art review of the technology, materials, properties & defects, and numerical modelling, J. Mater. Res. Technol., 20, pp. 2109–2172. DOI: https://doi.org/10.1016/j.jmrt.2022.07.121

[3] Rometsch, P.A., Zhu, Y., Wu, X., and Huang, A. (2022). Review of high-strength aluminium alloys for additive manufacturing by laser powder bed fusion, Mater. Des., 219, pp. 110779. DOI: 10.1016/j.matdes.2022.110779

[4] Zhao, L., Song, L., Santos Macías, J.G., Zhu, Y., Huang, M., Simar, A., and Li, Z. (2022). Review on the correlation between microstructure and mechanical performance for laser powder bed fusion AlSi10Mg, Addit. Manuf., 56, pp. 102914. DOI: https://doi.org/10.1016/j.addma.2022.102914

[5] Maleki, E., Bagherifard, S., Bandini, M., and Guagliano, M. (2021). Surface post-treatments for metal additive manufacturing: Progress, challenges, and opportunities, Addit. Manuf., 37, pp. 101619. DOI: https://doi.org/10.1016/j.addma.2020.101619

[6] Girelli, L., Tocci, M., Montesano, L., Gelfi, M., and Pola, A. (2018). Investigation of cavitation erosion resistance of AlSi10Mg alloy for additive manufacturing, Wear, 402–403, pp. 124–136. DOI: https://doi.org/10.1016/j.wear.2018.02.018

[7] Bagherifard, S., Beretta, N., Monti, S., Riccio, M., Bandini, M., and Guagliano, M. (2018). On the fatigue strength enhancement of additive manufactured AlSi10Mg parts by mechanical and thermal post-processing, Mater. Des., 145, pp. 28–41. DOI: https://doi.org/10.1016/j.matdes.2018.02.055

[8] Di Egidio, G., Martini, C., Ceschini, L., and Morri, A. (2023). Influence of electroless nickel–DLC (diamond-like carbon) multilayer coating on the mechanical performance of the heat-treated AlSi10Mg alloy produced by powder bed fusion–laser beam, Mater., 16 (9). DOI: https://doi.org/10.3390/ma16093313

[9] Sudagar, J., Lian, J., and Sha, W. (2013). Electroless nickel, alloy, composite and nano coatings – A critical review, J. Alloys Compd., 571, pp. 183–204. DOI: https://doi.org/10.1016/j.jallcom.2013.03.107

[10] Bewilogua, K., and Hofmann, D. (2014). History of diamond-like carbon films — From first experiments to worldwide applications, Surf. Coat. Technol., 242, pp. 214–225. DOI: https://doi.org/10.1016/j.surfcoat.2014.01.031

[11] Di Egidio, G., Martini, C., Ghassemali, E., and Morri, A. (2025). Electroless Ni-P + diamond-like carbon multilayer: Influence on tribological behaviour of AlSi10Mg produced by powder bed fusion – laser beam, Wear, 566–567, pp. 205803. DOI: https://doi.org/10.1016/j.wear.2025.205803

[12] Lee, C. K., Chen, C. H., and Tan, A. H. (2016). Electrochemical corrosion and wear behavior of an ultra-thin DLC film deposited on different annealing Ni-P layers on Al-Mg alloy in NaCl solution, Int. J. Electrochem. Sci., 11(7), pp. 5983–5998. DOI: https://doi.org/10.20964/2016.07.06

[13] Staia, M.H., Puchi Cabrera, E.S., Iost, A., Zairi, A., Belayer, S., and Van Gorp, A. (2015). Tribological response of AA 2024-T3 aluminium alloy coated with a DLC duplex coating, Tribol. Int., 85, pp. 74–87. DOI: https://doi.org/10.1016/j.triboint.2014.12.007

[14] Di Egidio, G., Abrami, M.B., Tonelli, L., Morri, A., Tocci, M., Pola, A., Ceschini, L., and Martini, C. (2026). Study of the critical issues related to the deposition of Ni-P + DLC multilayer coating on PBF-LB AlSi10Mg components with complex geometries and lattice structures, Prog Addit Manuf. DOI: https://doi.org/10.1007/s40964-025-01490-x
[15] ASTM G32-16. Standard test method for cavitation erosion using vibratory apparatus.
[16] Chahine, G., Kim, K. H., Franc, J. P., and Karimi, A. (2014). Advanced experimental and numerical techniques for cavitation erosion prediction, Springer. DOI: https://doi.org/10.1007/978-94-017-8539-6
[17] Lin, C.J., Chen, K.C., and He, J.L. (2006). The cavitation erosion behavior of electroless Ni–P–SiC composite coating, Wear, 261(11), pp. 1390–1396. DOI: https://doi.org/10.1016/j.wear.2006.03.054
[18] Park, I., and Kim, S. (2019). Cavitation erosion damage characteristics of electroless nickel plated gray cast iron, Acta Phys. Pol. A, 135, pp. 1018–1022. DOI: https://doi.org/10.12693/APhysPolA.135.1018
[19] Park, I.C., and Kim, S.J. (2019). Effect of stabilizer concentration on the cavitation erosion resistance characteristics of the electroless nickel plated gray cast iron in seawater, Surf. Coat. Technol., 376, pp. 31–37. DOI: https://doi.org/10.1016/j.surfcoat.2018.08.098
[20] Voevodin, A.A., Walck, S.D., and Zabinski, J.S. (1997). Architecture of multilayer nanocomposite coatings with super-hard diamond-like carbon layers for wear protection at high contact loads, Wear, 203–204, pp. 516–527.
[21] Cheng, F., and Jiang, S. (2014). Cavitation erosion resistance of diamond-like carbon coating on stainless steel, Appl. Surf. Sci., 292, pp. 16–26. DOI: https://doi.org/10.1016/j.apsusc.2013.11.044
[22] Cheng, F., Ji, W., and Zhao, J. (2019). Influence of adhesion strength on cavitation erosion resistance of diamond-like carbon coating, Ind. Lubr. Tribol., 71(5), pp. 724–730. DOI: https://doi.org/10.1108/ILT-01-2019-0024
[23] Cheng, F., Wu, F., Liu, L., Yang, S., and Ji, W. (2021). Investigation on cavitation erosion of diamond-like carbon films with heterogeneous multilayer structure, Surf. Coat. Technol., 405, pp. 126682. DOI: https://doi.org/10.1016/j.surfcoat.2020.126682
[24] Bai, L., Wu, P, Liu, H., Yan, J., Su, C. and Li, C. (2018).Rod-shaped cavitation bubble structure in ultrasonic field, Ultrason. Sonochem., 44, pp. 184-195. DOI: https://doi.org/10.1016/j.ultsonch.2018.02.030
[25] Li, H., Sun, P., and Cheng, D. (2021). Structure and properties of DLC films deposited on Mg alloy at different C2H2 flows of magnetron sputtering process, Coatings, 11. DOI: https://doi.org/10.3390/coatings11070815
[26] Franc, J. P., and Michel, J. M. (2005). Fundamentals of cavitation, Springer.
[27] Hattori, S., and Nakao, E. (2001). Cavitation erosion mechanisms and quantitative evaluation based on erosion particles, Wear, 249(10–11), pp. 839–845. DOI: https://doi.org/10.1016/S0043-1648(00)00308-2
[28] Abouel-Kasem, A., Emara, K.M., and Ahmed, S.M. (2009). Characterizing cavitation erosion particles by analysis of SEM images, Tribol. Int., 42(1), pp. 130–136. DOI: 10.1016/j.triboint.2008.05.008